engineering proceedings

MDPI

Proceeding Paper

Frequency Domain Modal Characterization and Multi-Injection Resonance Assessment of a Zeta DC–DC Converter †

Plamen Stanchev [1,2], Nikolay Hinov [1,3,*] and Reni Kabakchieva [1]

1 CoE "National Center of Mechatronics and Clean Technologies", 1000 Sofia, Bulgaria; p.stanchev@tu-sofia.bg (P.S.); reni.kabakchieva@tu-sofia.bg (R.K.)
2 Department of Intelligent Technology in Industry, Faculty of Computer Systems and Technologies, Technical University of Sofia, 1000 Sofia, Bulgaria
3 Department of Computer Systems, Faculty of Computer Systems and Technologies, Technical University of Sofia, 1000 Sofia, Bulgaria
* Correspondence: hinov@tu-sofia.bg
† Presented at the 15th International Scientific Conference TechSys 2026—Engineering, Technologies and Systems, Plovdiv, Bulgaria, 14–16 May 2026.

Abstract

This paper presents a frequency domain harmonic and modal analysis of a four-bus Zeta DC–DC converter, targeting the identification of resonance phenomena up to 200 MHz. The method is based on nodal admittance modeling and eigenvalue decomposition of the impedance matrix, enabling extraction of modal impedance and dominant resonance modes. Participation factors and sequential current injection at each bus are employed to evaluate spatial sensitivity and voltage amplification under different excitation scenarios. A two-stage frequency sweep, combining a coarse global scan with fine local refinement around detected peaks, ensures efficient and accurate resonance characterization. Simulation results demonstrate strong dependence of resonance severity on the injection location and highlight the dominant contribution of specific modes and reactive elements. The proposed framework provides physical insight and supports resonance-aware design of power electronic converters.

Keywords: Zeta DC–DC converter; harmonic analysis; modal impedance; resonance analysis; participation factors; power electronics; frequency domain modeling

1. Introduction

DC–DC converters are a fundamental element in modern electronic power systems, widely used in electric vehicles, renewable energy sources, industrial power supplies and high-frequency power electronics [1,2]. Among them, the Zeta DC–DC converter stands out for its ability to provide both step-up and step-down voltage conversion, with continuous input current and good compatibility with input filters [3]. These characteristics make it suitable for applications with high requirements for electromagnetic compatibility and power supply stability.

With the increase in operating frequencies and the integration of low-value passive elements, the dynamic behavior of DC–DC converters become increasingly sensitive to parasitic parameters and high-frequency resonance phenomena [4,5]. Such resonances can lead to significant amplification of voltages and currents in certain nodes, increased electromagnetic emissions and potential degradation of system reliability [6–9]. Therefore, identifying and understanding resonance mechanisms over a wide frequency range is a key aspect of designing reliable power electronic converters [10–12].

Academic Editors: Nikola G. Shakev, Valyo N. Nikolov, Nikolay R. Kakanakov and Sevil A. Ahmed-Shieva

Published: 21 July 2026

Classical approaches to the analysis of DC–DC converters are usually based on averaged models or linear small-signal representations, which are effective in the low-frequency range, but often do not adequately reflect the high-frequency behavior and modal structure of the system. In this context, frequency domain and matrix model-based methods provide a deeper physical insight into the interaction between individual elements and nodes in the circuit.

This paper presents a systematic harmonic and modal analysis of a four-node Zeta DC–DC converter from Texas Instruments, Dallas, USA, based on the nodal conductance matrix and the eigenvalues of the impedance matrix. By extracting modal impedances, dominant resonant modes and participation factors, the spatial sensitivity of the system to harmonic excitations is estimated. Additionally, the use of sequential current injection at each node allows a quantitative comparison of the resonant vulnerability of individual nodes and excitation scenarios.

The main contributions of this work can be summarized as follows:

- Development of a frequency-based modal model for the analysis of a Zeta DC–DC converter up to 200 MHz;
- Introduction of a two-step frequency scanning procedure for efficient detection of resonance peaks;
- Estimation of the resonance sensitivity by combining contribution factors and multi-injection analysis;
- Provision of a physical interpretation of the observed resonances relevant for the design and optimization of power electronic systems.

2. Mathematical Models

2.1. Nodal Representation of the Zeta DC–DC Converter

For the purpose of harmonic and modal analysis, the Zeta DC–DC converter is represented by a linearized small-signal model in the frequency domain. The circuit is reduced to an equivalent four-node passive network including active resistances, inductances, capacitances and load, with the parasitic parameters of the key element and the diode explicitly taken into account. Let the vector of node voltages be defined as:

$$\mathbf{V}(\omega) = \begin{bmatrix} V_1(\omega) & V_2(\omega) & V_3(\omega) & V_4(\omega) \end{bmatrix}^T \tag{1}$$

and the vector of the nodal currents as:

$$\mathbf{I}(\omega) = \begin{bmatrix} I_1(\omega) & I_2(\omega) & I_3(\omega) & I_4(\omega) \end{bmatrix}^T \tag{2}$$

In the frequency domain ($\omega = 2\pi f$) the dynamics of the system is described by the classical nodal equation:

$$\mathbf{I}(\omega) = \mathbf{Y}(\omega) \cdot \mathbf{V}(\omega) \tag{3}$$

where $\mathbf{Y}(\omega)$ is the complex nodal matrix of conductivities.

2.2. Construction of the Nodal Admittance Matrix

The matrix $\mathbf{Y}(\omega)$ is constructed directly from the frequency-dependent impedances and conductivities of the elements in the circuit. The series branches (switch, inductances) are modeled by:

$$Z_L(\omega) = R + j\omega L \tag{4}$$

and the parallel capacitive elements by:

$$Y_C(\omega) = j\omega C \tag{5}$$

According to the adopted nodal structure of the Zeta converter, the nodal matrix has the form:

$$\mathbf{Y}_C(\omega) = \begin{bmatrix} y_{11} & -y_{12} & 0 & 0 \\ -y_{21} & y_{22} & -y_{23} & 0 \\ 0 & -y_{32} & y_{33} & -y_{34} \\ 0 & 0 & -y_{43} & y_{44} \end{bmatrix} \tag{6}$$

where the diagonal elements represent the sum of all conductance's connected to the corresponding node, and the off-diagonal elements, the negative values of the intermediate branch conductance's. This form provides energy consistency and a correct description of the interconnection between the nodes.

2.3. Impedance Matrix and Harmonic Response

By inverting the nodal matrix, the frequency-dependent impedance matrix is obtained:

$$\mathbf{Z}(\omega) = \mathbf{Y}^{-1}(\omega) \tag{7}$$

which directly relates the nodal voltages and currents:

$$\mathbf{V}(\omega) = \mathbf{Z}(\omega) \cdot \mathbf{I}(\omega) \tag{8}$$

This formulation allows for the analysis of the harmonic response of the system under arbitrary nodal current excitation and serves as the basis for the multi-injection analysis used in this study.

2.4. Modal Decomposition of the Impedance Matrix

The resonant properties of the system are investigated by eigen decomposition of the impedance matrix:

$$\mathbf{Z}(\omega) = T(\omega)D(\omega)L^T(\omega) \tag{9}$$

where $D(\omega)$ is a diagonal matrix containing the modal impedances $\lambda_i(\omega)$, $T(\omega)$, and $L(\omega)$ are the right and left eigenvectors, respectively.

The modal impedances $|\lambda_i(\omega)|$ provide direct information about the resonances of the system, with the dominant mode at a given frequency defined as:

$$i^*(\omega) = \underset{i}{\operatorname{argmax}} |\lambda_i(\omega)| \tag{10}$$

2.5. Participation Factors

To quantify the influence of each node on a given resonant mode, Participation Factors (PF) are used. For the dominant mode i^*, the participation factor of node k is defined as:

$$PF = \left| L_{k,i^*} T_{i^*,k} \right| \tag{11}$$

For the purposes of comparative analysis, the participation factors are normalized such that:

$$\sum_{k=1}^{N} PF_k^{\text{norm}} = 1 \tag{12}$$

This allows a clear interpretation of the spatial distribution of the resonant energy in the circuit.

https://doi.org/10.3390/engproc2026150048

2.6. Multi-Injection Harmonic Analysis

In contrast to the classical analysis with a single excitation, in the present work a sequential current injection is used at each node. This is implemented by means of an excitation matrix:

$$\mathbf{I}_{inj} = I_0 \mathbf{I}_N \tag{13}$$

where I_0 is the amplitude of the injected current, and $\mathbf{I}_N$ is the identity matrix.

In this way, the full voltage response matrix is obtained:

$$\mathbf{V}(\omega) = \mathbf{Z}(\omega) I_{inj} \tag{14}$$

which allows comparison of the resonant sensitivity under different excitation scenarios, identification of the most vulnerable nodes, assessment of the most critical "injection-node" combinations.

2.7. Summary of the Modeling Framework

The presented mathematical model combines nodal analysis, impedance description, and modal decomposition into a single frequency-based framework. This approach allows for a systematic study of the resonance phenomena in the Zeta DC–DC converter over a wide frequency range and serves as the basis for the numerical simulations and results presented in the following sections.

3. Numerical Simulations and Results

This section presents the numerical simulation results obtained from the proposed modal-based harmonic analysis of the four-bus Zeta DC–DC converter. The objective of the simulations is to investigate the resonance behavior, voltage amplification, and harmonic vulnerability of the system over a wide frequency range, extending up to 200 MHz.

Table 1 summarizes the electrical parameters of the four-bus Zeta DC–DC converter used in the harmonic and modal analysis. The model includes parasitic resistances and inductances of the switching device and inductive elements, as well as the coupling and output capacitors, in order to accurately capture high-frequency dynamics. The inclusion of the diode parasitic capacitance and load resistance allows the representation of realistic operating conditions and resonance behavior beyond the low-frequency range. All parameters correspond to typical values used in medium-power DC–DC converter applications and are assumed to be constant over the analyzed frequency range.

Table 2 presents the main simulation settings and frequency sweep conditions adopted in this study. A two-stage frequency domain analysis is employed, consisting of a coarse sweep over a wide frequency range up to 200 MHz, followed by localized fine sweeps around the detected resonance peaks. This approach significantly reduces computational cost while preserving high resolution in the vicinity of critical resonances. Sequential current injection at each bus is applied to evaluate spatial sensitivity and worst-case voltage amplification. The dominant resonance modes, participation factors, and voltage responses are extracted at each frequency point to enable comprehensive resonance characterization.

The analysis combines nodal impedance modeling, eigenvalue-based modal decomposition, participation factor evaluation, and multi-point current injection. This integrated approach enables a systematic comparison of resonance characteristics as a function of frequency and injection location, providing both global and localized insight into the dynamic behavior of the converter.

The results are illustrated through a set of complementary plots, including dominant modal impedance trends, bus voltage responses, worst-case voltage envelopes, injection severity maps, and Bode-like representations. Together, these figures reveal the relationship between modal dominance, spatial voltage distribution, and resonance sensitivity, forming a comprehensive basis for discussion and design-oriented interpretation.

Table 1. Zeta DC–DC Converter Parameters.

Parameter	Symbol	Value	Description
Switch resistance	R_q	55 mΩ	On-state resistance of the switching device
Switch inductance	L_q	50 nH	Parasitic inductance of the switch
Input capacitor	C_{in}	24.7 µF	Input filter capacitor
Inductor L1a resistance	$R_{L1}a$	100 mΩ	Series resistance of input inductor
Inductor L1a inductance	L_{1a}	17 µH	Input-side inductor
Coupling capacitor	C_c	4.7 µF	Energy transfer capacitor
Diode parasitic capacitance	C_d	1 pF	High-frequency parasitic capacitance
Inductor L1b resistance	R_{L1b}	100 mΩ	Series resistance of output inductor
Inductor L1b inductance	L_{1b}	17 µH	Output-side inductor
Output capacitor	C_{out}	24.7 µF	Output filter capacitor
Load resistance	R_{load}	144	Resistive load

Table 2. Simulation and Frequency Sweep Conditions.

Parameter	Symbol	Value	Description
Frequency range	f	1 kHz–200 MHz	Harmonic analysis bandwidth
Coarse frequency step	Δf_c	1 Hz	Initial resonance detection
Fine sweep bandwidth	—	±1 MHz	Local refinement around peaks
Fine frequency step	Δf_f	1 Hz	High-resolution resonance analysis
Current injection amplitude	I_{inj}	1 A	Small-signal excitation
Injection strategy	—	Sequential per bus	Resonance sensitivity comparison
Dominant mode criterion	—	max(λ)	Selection of resonance mode
Peak detection threshold	—	2% of max(λ)	Prominence-based peak detection

Figure 1 shows the dependence of the dominant modal impedance $|\lambda|$ on frequency in the range up to 200 MHz. A monotonic increase of $|\lambda|$ with increasing frequency is observed, which indicates that the equivalent impedance of the dominant mode becomes larger in the high-frequency range (influence of reactive elements).

At the very beginning of the range, a strongly pronounced peak is visible at very low frequencies, which is "compressed" towards zero due to the scale of the frequency axis. This behavior is usually an indicator of quasi-resonance/near-singularity of $Z(\omega)$ in the low-frequency region (or a numerical singularity near DC), therefore, for a clearer interpretation of low frequencies, a logarithmic (Bode-like) scale and a separate zoom in the initial range are appropriate.

Figure 2 shows the modal impedances |λm| of the matrix $Z(\omega) = Y(\omega) - 1$ for the four eigenmodes of the 4-node Zeta model. It is clearly seen that Mode 1 dominates the entire frequency range considered, with its modal impedance increasing almost linearly with frequency. This indicates that the dynamics of the system are mainly determined by this mode and that the remaining modes have a significantly smaller contribution to the total impedance. Modes 2–4 remain practically negligible compared to Mode 1 and are visually "fused" to the axis, meaning that they do not significantly participate in the resonant behavior in this frequency range. This strong separation of the modal impedances confirms that the system can be effectively analyzed by a dominant modal approach, which simplifies the interpretation of the resonances and the participation of individual nodes.

https://doi.org/10.3390/engproc2026150048

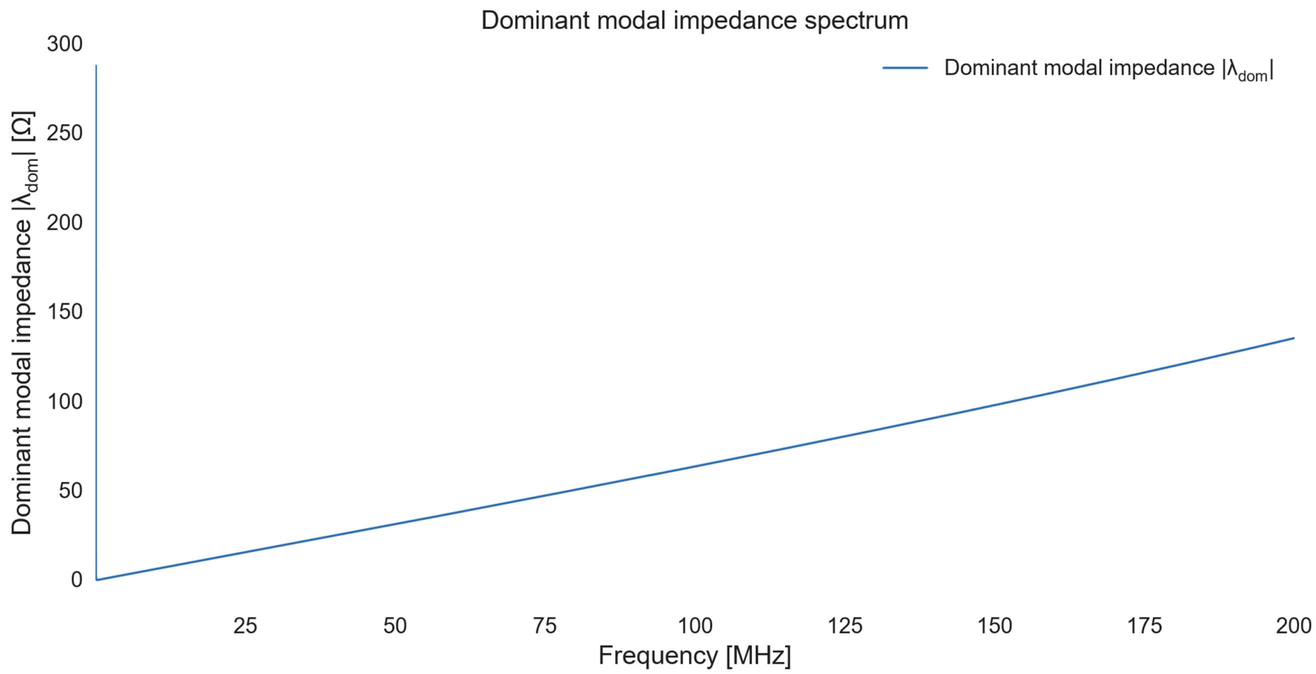

Figure 1. Frequency response of the dominant modal impedance $|\lambda_{\text{dom}}|$ of the 4-bus Zeta DC-DC converter.

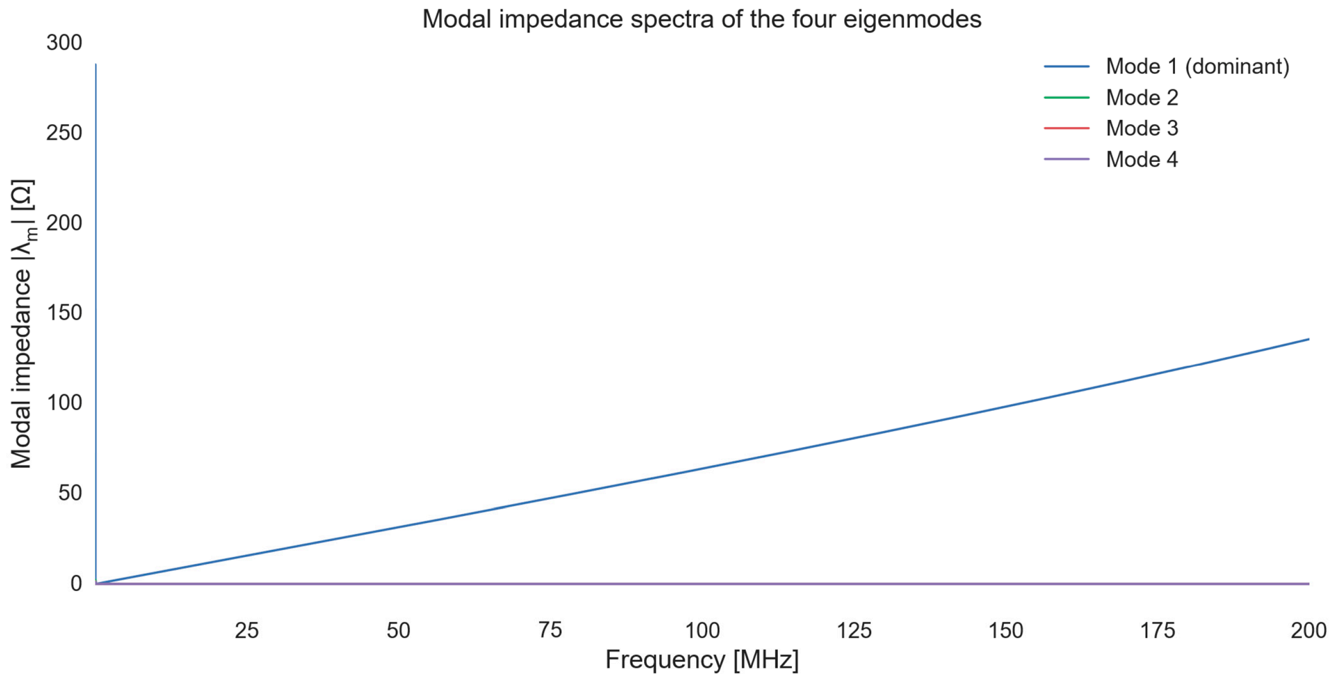

Figure 2. Modal impedances $|\lambda_m|$ of the nodal impedance matrix $Z(\omega) = Y(\omega)^{-1}$ for the 4-bus Zeta model.

Figure 3 illustrates the magnitude of the bus voltage responses $|V|$ as a function of frequency when a unit current is injected at Bus 2.

It can be observed that the voltage response remains negligible over most of the frequency range, indicating a well-damped behavior at low and mid frequencies. However, a pronounced high-frequency resonance emerges close to the upper end of the analyzed spectrum (around the hundreds of MHz range), where significant voltage amplification is observed.

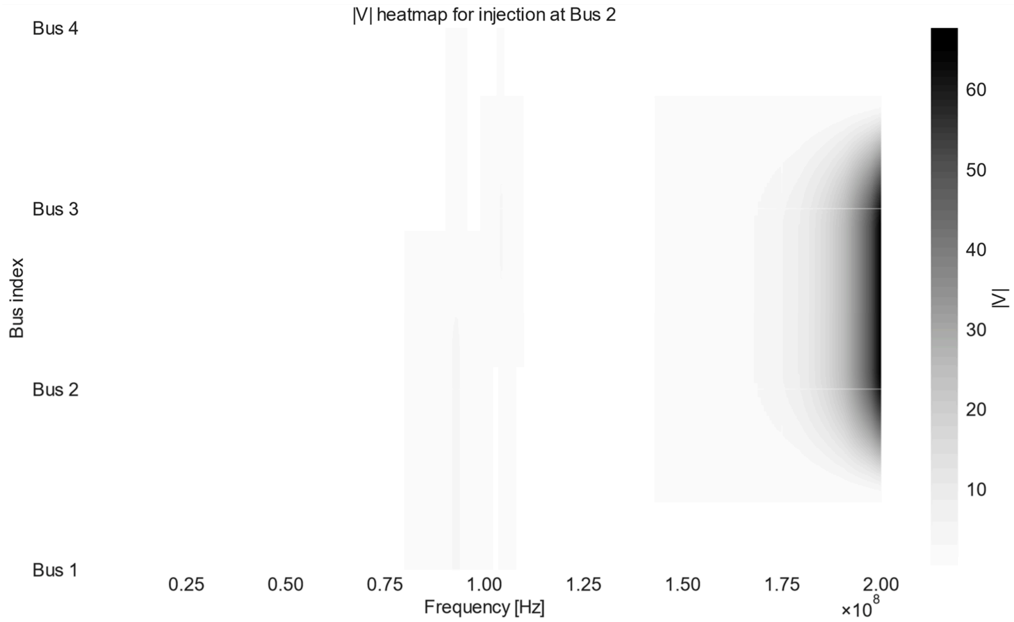

Figure 3. Bus voltage amplification and high-frequency resonance for injection at Bus 2.

The resonance is not uniformly distributed across all buses. Instead, Bus 3 and Bus 4 exhibit the highest voltage magnitudes, revealing a strong coupling between the injection point (Bus 2) and the downstream nodes of the Zeta converter. This behavior highlights the dominant role of the output-side reactive elements in shaping the high-frequency resonance and identifies the most vulnerable buses under harmonic current excitation.

Figure 4 presents the worst-case voltage envelope, defined as the maximum voltage magnitude observed across all buses and all injection locations as a function of frequency.

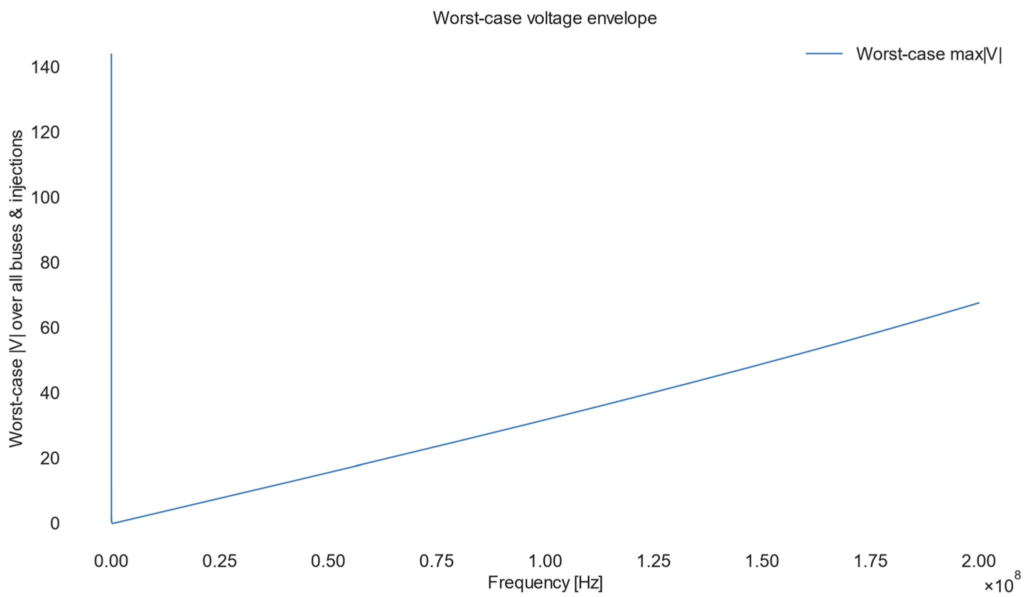

Figure 4. Worst-case voltage envelope over all buses and injection locations.

It can be seen that the worst-case response increases almost monotonically with frequency, indicating a progressive loss of harmonic robustness in the high-frequency range.

Similar to the behavior observed in the dominant modal impedance (Figure 1), a sharp peak appears at very low frequencies, which is compressed near the origin due to the linear frequency scale. Beyond this region, the envelope grows steadily, revealing that high-frequency excitation leads to increasingly severe voltage amplification regardless of the injection location.

Importantly, this figure provides a conservative upper bound on the expected voltage magnitudes in the system. It therefore serves as a practical indicator for identifying critical frequency ranges where the Zeta converter is most vulnerable to harmonic disturbances.

Figure 5 illustrates the injection severity as a function of frequency, expressed as the maximum voltage magnitude observed across all buses for a given injection location.

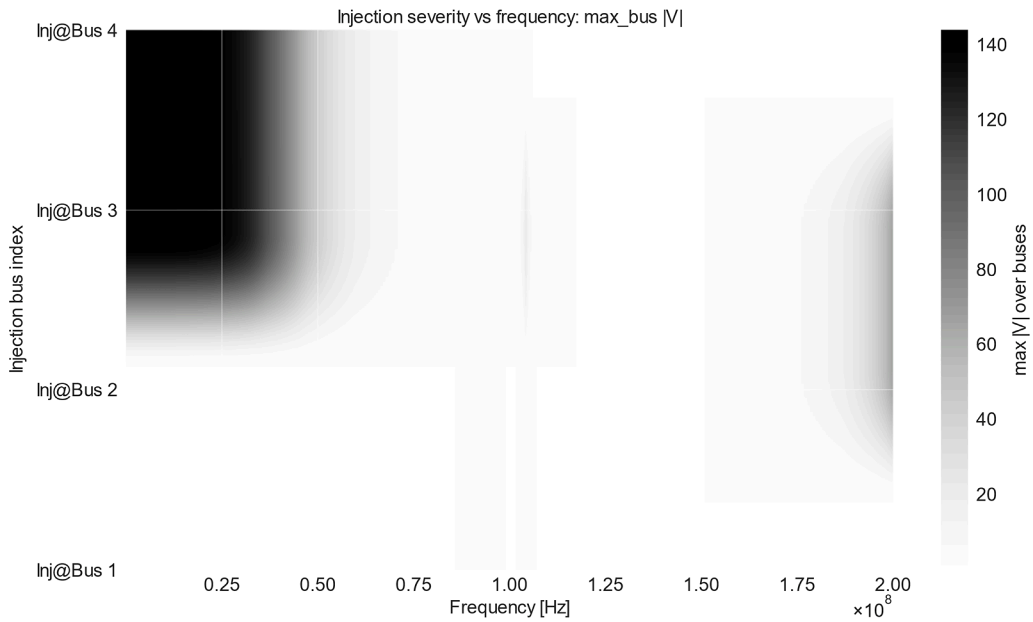

Figure 5. Injection severity versus frequency: maximum bus voltage response.

Each row corresponds to a different injection bus, while the color intensity represents the worst-case voltage response in the network.

The results clearly indicate that the severity of harmonic excitation strongly depends on the injection location. In particular, injections at Bus 3 and Bus 4 lead to significantly higher voltage amplification in the low-frequency region, as evidenced by the dark regions in the heatmap. This behavior suggests a strong coupling between these buses and the dominant resonant modes of the system.

In contrast, injections at Bus 1 and Bus 2 exhibit considerably lower impact over most of the frequency range, indicating a more benign interaction with the network dynamics. At higher frequencies, a gradual increase in severity is observed for all injection locations, consistent with the trends identified in the dominant modal impedance and worst-case envelope.

Overall, this figure highlights that both frequency and injection location are critical factors in determining the harmonic vulnerability of the Zeta converter.

Figure 6 shows the index of the most affected bus as a function of frequency and injection location, defined as the bus at which the maximum voltage magnitude occurs for a given injection.

Each row corresponds to an injection bus, while the color encodes the index of the bus experiencing the highest voltage response.

The figure reveals a clear frequency-dependent migration of the worst observed bus, indicating that resonant energy is redistributed across the network depending on both excitation frequency and injection location. In the low-frequency range, the worst response is primarily localized near the injection point, whereas at higher frequencies the maximum voltage shifts toward downstream buses, most notably Bus 4.

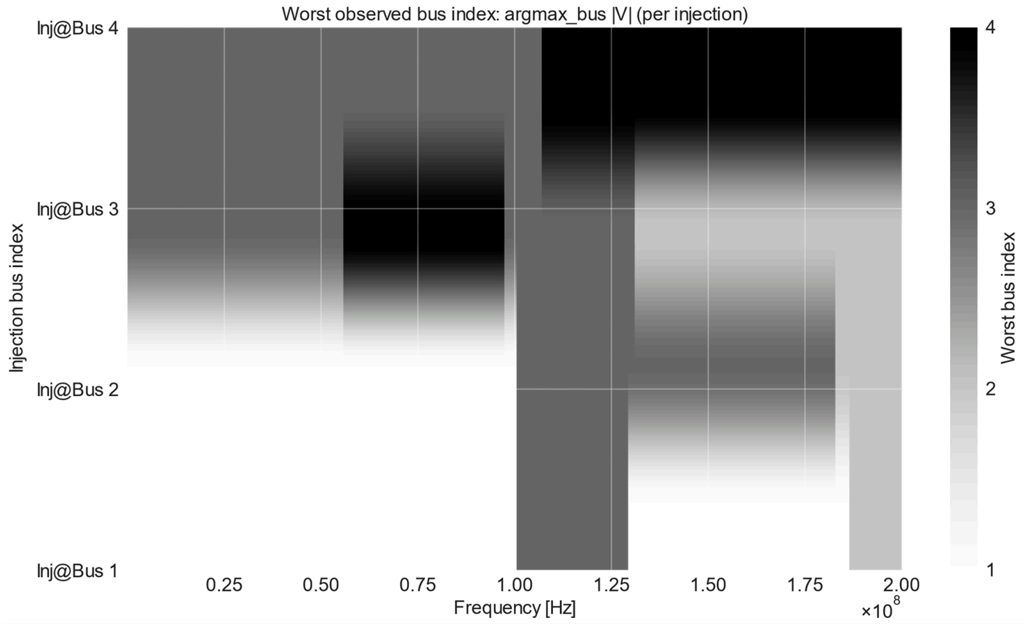

Figure 6. Worst observed bus index versus frequency and injection location.

This behavior highlights the presence of frequency-dependent mode shapes, where different buses dominate the system response at different resonance bands. As a result, the most vulnerable bus cannot be identified solely based on topology or proximity to the excitation source, but must be determined through frequency domain analysis.

Overall, this figure complements the injection severity map (Figure 5) by indicating where the most critical voltages appear in the system for each excitation scenario.

Figure 7 presents the normalized PF of the dominant mode as a function of frequency for each bus.

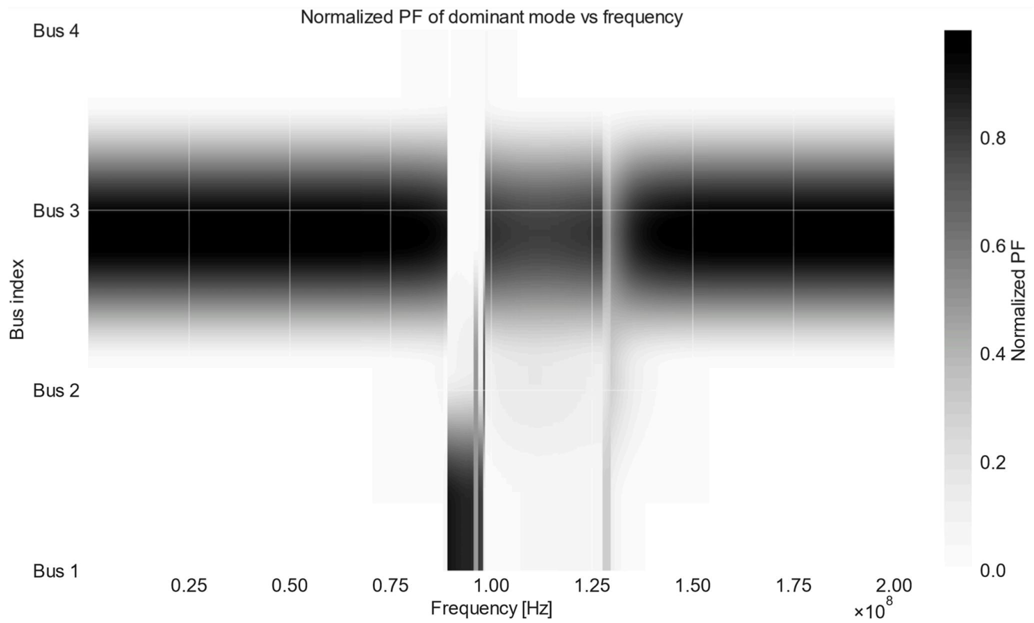

Figure 7. Normalized participation factors of the dominant mode versus frequency.

The color intensity represents the relative contribution of each bus to the dominant resonant mode, normalized such that the sum of PFs equals unity at each frequency.

The results reveal a clear frequency-dependent redistribution of modal participation among the buses. In the low-frequency range, the dominant mode is primarily associated with Bus 3, indicating that this node plays a leading role in shaping the system's resonant behavior. Around the transition region near 100 MHz, a sharp change in participation is observed, corresponding to a modal crossover.

At higher frequencies, the dominant participation gradually shifts toward Bus 4, explaining the increased voltage amplification and vulnerability observed at this node in Figures 5 and 6. This confirms that the spatial distribution of resonance effects is governed by the underlying modal structure rather than by the injection location alone.

Overall, this figure provides the modal explanation for the injection severity and worst-bus maps, demonstrating a strong correlation between dominant-mode participation factors and observed voltage amplification patterns.

Figure 8 compares the resonance response for different injection locations, expressed as the maximum voltage magnitude observed across all buses for each injection as a function of frequency.

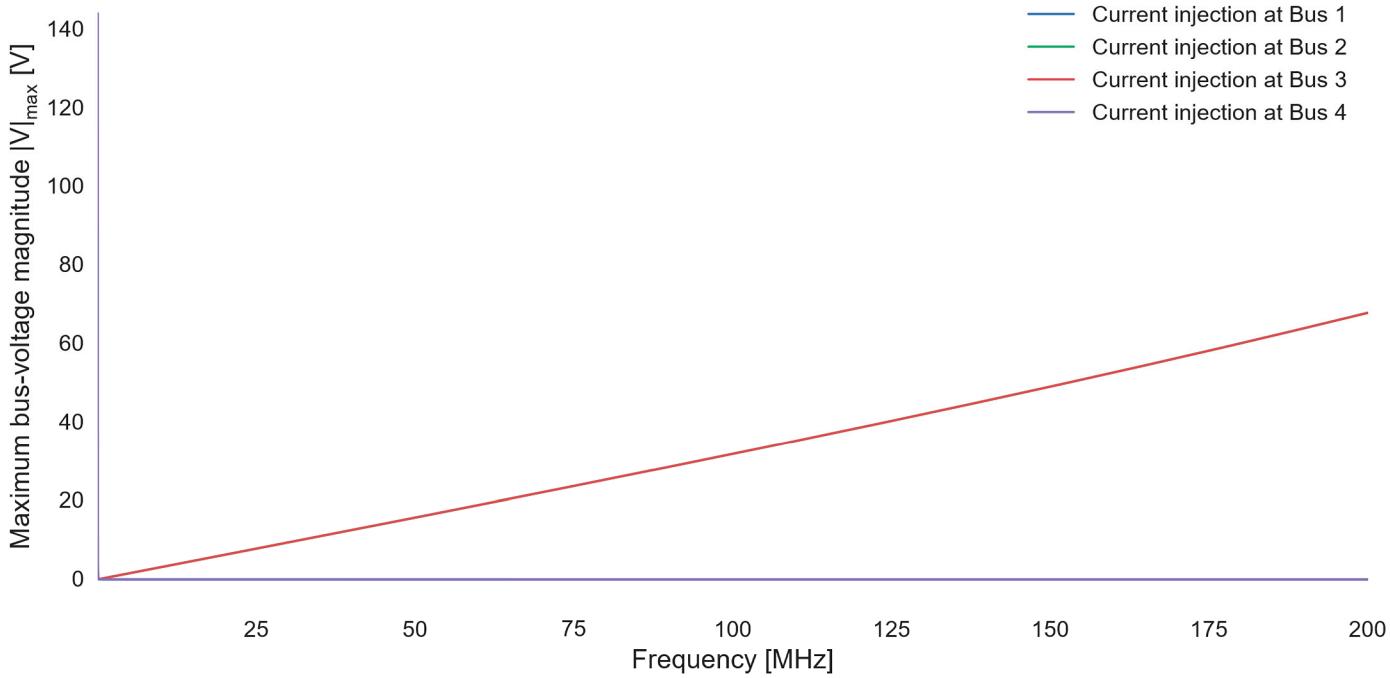

Figure 8. Resonance comparison per injection location: maximum bus voltage response.

Each curve corresponds to a single injection bus, allowing a direct comparison of how strongly each excitation location couples to the resonant dynamics of the system.

The results demonstrate a pronounced disparity between injection locations. Injections at Bus 3 and Bus 4 produce significantly higher voltage amplification over a wide frequency range, with the response increasing steadily toward higher frequencies. This indicates strong coupling of these buses to the dominant resonant modes identified in Figures 1 and 7.

In contrast, injections at Bus 1 and Bus 2 result in negligible voltage amplification across most of the spectrum, suggesting a weak interaction with the system's resonant structure. The sharp low-frequency spike visible for some injections corresponds to the low-frequency resonance compressed near the origin on the linear frequency scale.

Overall, this figure confirms that the resonance behavior of the Zeta converter is highly injection-location-dependent, and that certain buses act as critical excitation points capable of triggering severe system-wide voltage amplification.

Figure 9 presents a Bode-like representation of the resonance behavior for different injection locations, expressed as the maximum bus voltage magnitude in decibels as a function of frequency.

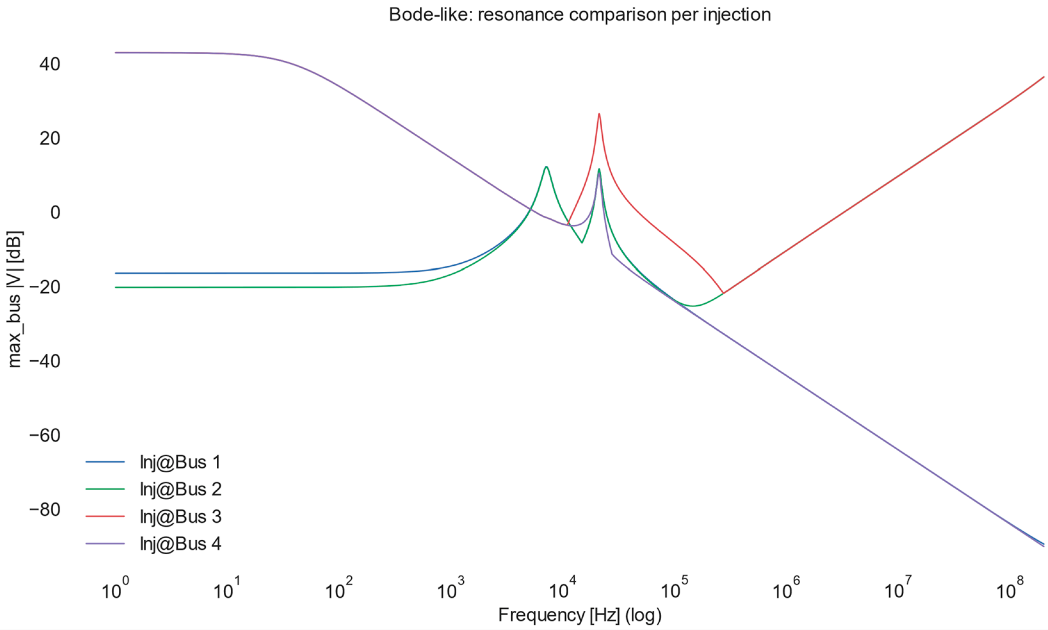

Figure 9. Bode-like resonance comparison per injection location.

Each curve corresponds to a single injection bus, enabling a clear comparison of resonance strength and bandwidth on a logarithmic frequency scale.

The logarithmic representation reveals several important features that are less evident in linear plots. First, multiple resonance peaks become clearly distinguishable in the mid-frequency range, particularly for injections at Bus 3 and Bus 4, confirming their strong coupling to the dominant system modes. These peaks correspond to the modal transitions and participation factor shifts identified in Figures 1 and 7.

Second, the magnitude and slope of the curves differ substantially between injection locations. Injections at Bus 1 and Bus 2 remain well below 0 dB over most of the frequency range, indicating limited voltage amplification. In contrast, injections at Bus 3 exhibit pronounced resonant amplification, while Bus 4 shows broadband sensitivity, especially at lower frequencies.

Finally, the Bode-like plot highlights the wide frequency span over which resonance effects can be significant, emphasizing that harmonic vulnerability in the Zeta converter is not confined to narrow frequency bands but can extend over several decades.

The peaks in Figure 9 are due to the dominant mode. They are strongest when the current injection is applied to a bus with a high participation factor for that mode. Therefore, Bus 3 and Bus 4 provide the strongest amplification, while Bus 1 and Bus 2 have a weaker effect.

4. Discussion

The results clearly demonstrate that the harmonic behavior of the four-bus Zeta converter is dominated by a single modal impedance over the majority of the investigated frequency range. As shown in Figures 1 and 2, the dominant eigenvalue of the nodal impedance matrix increases monotonically with frequency, while the remaining modes remain comparatively suppressed. This indicates a strong modal decoupling, where one mode governs the high-frequency response of the system.

The absence of multiple competing dominant modes simplifies the resonance interpretation but simultaneously highlights the risk of pronounced voltage amplification when the dominant mode aligns with external excitation. In particular, the sharp increase in the dominant modal impedance at very low frequencies and its steady growth toward the high-frequency range suggest that both low-frequency dynamics and parasitic high-frequency effects must be considered in the converter design.

The voltage heatmap in Figure 3 reveals a highly non-uniform spatial distribution of voltage magnitudes under current injection at Bus 2. While lower frequencies exhibit relatively low and evenly distributed voltage levels, a pronounced amplification emerges close to the upper end of the frequency range. This behavior indicates that the resonance is not only frequency-selective but also spatially localized.

Figure 4 further confirms this observation by presenting the worst-case voltage envelope across all buses and injection points. The envelope follows a similar trend to the dominant modal impedance, reinforcing the strong correlation between modal dominance and voltage amplification. This validates the use of modal impedance magnitude as a reliable indicator for identifying critical resonance regions.

A key contribution of this work lies in the systematic comparison of resonance severity under sequential current injection at each bus. Figure 5 demonstrates that the resonance strength is strongly dependent on the injection location, with injections at Buses 3 and 4 producing significantly higher voltage amplification compared to Buses 1 and 2.

This observation is further clarified in Figure 6, which maps the worst observed bus index for each injection and frequency. The results show that certain buses consistently act as "victims" of resonance, regardless of where the disturbance is applied. Such behavior reflects the intrinsic topology and energy storage distribution of the Zeta converter, rather than a purely local effect.

The normalized PF map in Figure 7 provides crucial insight into the physical origin of the observed resonances. Across wide frequency regions, a single bus exhibits dominant participation in the governing mode, indicating that the resonance energy is primarily associated with specific reactive elements connected to that node.

The abrupt changes in participation around certain frequencies coincide with transitions in the dominant mode index and resonance peaks, confirming that modal interaction plays a decisive role in shaping the system's harmonic response. This behavior supports the interpretation that high-frequency resonances are driven by parasitic capacitances and inductive branches, while lower-frequency behavior is governed by bulk energy storage elements.

Figures 8 and 9 summarize the resonance behavior from an injection-centric perspective. The linear-scale comparison (Figure 8) highlights the absolute severity differences between injection points, whereas the Bode-like representation (Figure 9) emphasizes relative amplification in decibel scale over several decades of frequency.

The Bode-like plots clearly show that different injection locations excite the dominant mode with varying efficiency, leading to distinct resonance peaks and slopes. This result underscores that resonance risk assessment based on a single excitation point may be misleading, and that multi-injection analysis is essential for robust converter evaluation.

From a design perspective, the presented results indicate that resonance mitigation strategies should prioritize buses with high modal participation and high vulnerability, rather than focusing solely on the injection source. Damping networks, layout optimization, or targeted component tuning at these critical nodes are expected to be more effective than uniform mitigation approaches.

https://doi.org/10.3390/engproc2026150048

Moreover, the proposed two-stage frequency sweep combined with modal metrics provides an efficient and scalable framework for identifying critical resonance regions in complex power electronic systems.

5. Conclusions

This paper presented a comprehensive modal-based harmonic analysis framework for a four-bus Zeta DC–DC converter, combining nodal impedance modeling, eigenvalue decomposition, participation factor evaluation, and multi-point current injection. The proposed methodology enables systematic identification and interpretation of resonance phenomena over a wide frequency range extending up to 200 MHz.

The numerical results demonstrated that the harmonic behavior of the Zeta converter is predominantly governed by a single dominant mode across most of the analyzed spectrum. This dominant modal impedance shows a strong correlation with voltage amplification and worst-case envelope trends, confirming its suitability as a compact and physically meaningful resonance indicator.

By introducing sequential current injection at each bus, the study revealed that resonance severity is highly dependent on the excitation location. In particular, injections at intermediate and output-side buses were shown to induce significantly higher voltage amplification compared to input-side excitations. This finding highlights the importance of considering spatial excitation diversity when assessing harmonic vulnerability in multi-node power electronic systems.

The participation factor analysis provided additional insight into the physical origin of the resonances, linking dominant modes to specific nodes and associated reactive elements. Abrupt changes in participation around resonance frequencies indicate modal transitions and underline the role of parasitic components in shaping high-frequency behavior.

Furthermore, the two-stage frequency sweep strategy proved effective in efficiently capturing both global resonance trends and localized high-Q peaks, while maintaining computational tractability. The resulting Bode-like representations and heatmap visualizations offer intuitive tools for resonance comparison, vulnerability assessment, and design-oriented interpretation.

Overall, the proposed framework extends conventional impedance-based analysis by incorporating modal dominance, spatial sensitivity, and multi-injection perspectives. The approach is general and can be readily applied to other DC–DC converter topologies and multi-node power electronic systems, supporting more robust resonance-aware design and mitigation strategies.

Author Contributions: Conceptualization, N.H., R.K. and P.S.; Methodology, N.H. and P.S.; Software, R.K. and P.S.; Validation, P.S.; Formal analysis, N.H., R.K. and P.S.; Investigation, P.S.; Resources, R.K. and P.S.; Data curation, P.S.; Writing—original draft, R.K. and P.S.; Writing—review and editing, N.H., R.K. and P.S.; Visualization, N.H., R.K. and P.S.; Supervision, N.H. and P.S.; Project administration, N.H.; Funding acquisition, N.H. All authors have read and agreed to the published version of the manuscript.

Funding: This work was supported by the European Regional Development Fund under the "Research In-novation and Digitization for Smart Transformation" program 2021–2027 under Project BG16RFPR002-1.014-0006 "National Centre of Excellence Mechatronics and Clean Technologies", and the APC was funded by Project BG16RFPR002-1.014-0006.

Institutional Review Board Statement: Not applicable.

Informed Consent Statement: Not applicable.

Data Availability Statement: The original contributions presented in this study are included in the article. Further inquiries can be directed to the corresponding author.

Conflicts of Interest: The authors declare no conflicts of interest.

Abbreviations

The following abbreviations are used in this manuscript:

PF	Participation Factors

References

1. Erickson, R.W.; Maksimović, D. *Fundamentals of Power Electronics*, 3rd ed.; Springer: Cham, Switzerland, 2020; pp. 1–10.
2. Forouzesh, M.; Siwakoti, Y.P.; Gorji, S.A.; Blaabjerg, F.; Lehman, B. Step-Up DC–DC Converters: A comprehensive review of Voltage-Boosting Techniques, Topologies, and applications. *IEEE Trans. Power Electron.* **2017**, *32*, 9143–9178. [CrossRef]
3. Górecki, P.; Górecki, K. Methods of Fast Analysis of DC–DC Converters—A Review. *Electronics* **2021**, *10*, 2920. [CrossRef]
4. Zhang, M.; Wang, J.; Zhang, S.; Gao, L.; Guo, X.; Chen, L.; Xu, Y. Harmonic resonance analysis and impedance remodeling method of Multi-Inverter Grid-Connected system. *Electronics* **2023**, *12*, 3684. [CrossRef]
5. Wang, X.; Blaabjerg, F. Harmonic Stability in Power Electronic-Based Power Systems: Concept, Modeling, and analysis. *IEEE Trans. Smart Grid* **2018**, *10*, 2858–2870. [CrossRef]
6. Sakinci, Ö.C.; Lekić, A.; Beerten, J. Generalized impedance-based AC/DC power system modeling for harmonic stability analysis. *Int. J. Electr. Power Energy Syst.* **2022**, *143*, 108456. [CrossRef]
7. Ma, Y.; Suo, L.; Guo, Y. MMC impedance modeling and system stability research based on harmonic state space theory. In Proceedings of the 6th International Conference on Electrical, Electronic Information and Communication Engineering (EEICE 2025), Shenzhen, China, 18–20 April 2025.
8. Becker, J.K.M.; Kettner, A.M.; Zuo, Y.; Cecati, F.; Pugliese, S.; Liserre, M.; Paolone, M. Modelling of AC/DC interactions of Converter-Interfaced resources for harmonic Power-Flow studies in microgrids. *arXiv* **2022**. [CrossRef]
9. Kong, R.; Sahoo, S.; Liu, Y.; Blaabjerg, F. Data-Driven Stability Assessment of Power Electronic Converters with Multi-Resolution Dynamic Mode Decomposition. *arXiv* **2024**. [CrossRef]
10. Arevalo-Soler, J.; Moutevelis, D.; Mateu-Barriendos, E.; Alican, O.; Collados-Rodriguez, C.; Cheah-Mañe, M.; Prieto-Araujo, E.; Gomis-Bellmunt, O. A Matlab-based toolbox for automatic EMT modeling and Small-Signal stability analysis of modern power systems. *arXiv* **2025**. [CrossRef]
11. Salles, R.S.; Rönnberg, S.K. Harmonic impedance studies of Swedish railway power system using wide-area modeling approach. *Railw. Eng. Sci.* **2026**, *34*, 1–23. [CrossRef]
12. Todorov, G.; Kamberov, K.; Ivanov, T. Parametric Optimisation of Resistance Temperature Detector Design Using Validated Virtual Prototyping Approach. *Case Stud. Therm. Eng.* **2021**, *28*, 101302. [CrossRef]

https://doi.org/10.3390/engproc2026150048